Step-by-Step Maturation Mechanism of Binary Toxin Pore Revealed by Cryo-EM Analysis

Tomohito Yamada[1#], Yukihiko Sugita[2,3,4], Toru Yoshida[1,5], Takeshi Noda[2,3], and Hideaki Tsuge[1,6,7#]

1. Faculty of Life Sciences, Kyoto Sangyo University, Kamigamo-motoyama, Kita-ku, Kyoto, 603-8555, Japan
2. Laboratory of Ultrastructural Virology, Institute for Life and Medical Sciences, Kyoto University, 53 Shogoin Kawahara-cho, Sakyo-ku, Kyoto 606-8507, Japan
3. Laboratory of Ultrastructural Virology, Graduate School of Biostudies, Kyoto University, 53 Shogoin Kawahara-cho, Sakyo-ku, Kyoto 606-8507, Japan
4. Hakubi Center for Advanced Research, Kyoto University, 53 Kawahara-cho, Shogoin, Sakyo-ku, Kyoto 606-8507, Japan
5. Department of Chemical and Biological Sciences, Faculty of Science, Japan Women's University, 2-8-1 Mejirodai, Bunkyo-ku, Tokyo, 112-8681, Japan
6. Institute for Protein Dynamics, Kyoto Sangyo University, Kamigamo-motoyama, Kita-ku, Kyoto, 603-8555, Japan
7. Center for Molecular Research in Infectious Diseases, Kyoto Sangyo University, Kamigamo-motoyama, Kita-ku, Kyoto, 603-8555, Japan

#Corresponding authors

Tomohito Yamada, t.mountain.rf23doc@gmail.com

Hideaki Tsuge, tsuge@cc.kyoto-su.ac.jp

Abstract

Membrane pore-forming proteins (PFPs) form ring-shaped membrane-translocating oligomers on membranes, contributing to infection, immunity, and cell death functions. Binary toxins produced by some bacteria consist of an enzymatic component that acts as a toxin and a membrane-binding component that forms a pore that delivers the enzymatic component into target cells. Cryo-electron microscopy (cryo-EM) has advanced our understanding of these translocation mechanisms by revealing several binary toxin complexes' structures. However, the mechanisms underlying the initial pore formation remain unclear. We determined the structures of several oligomeric forms of the membrane-binding component, Ib, of the Iota toxin from *Clostridium perfringens* at various stages of pore formation. Structural comparisons revealed that the symmetrically arranged soluble oligomer (prepore) became a transmembrane oligomer (pore). These findings enhance our understanding of the PFP mechanisms and provide a structural basis for developing nanodevices using membrane pores.

Membrane pore-forming proteins (PFPs) are a family of proteins produced by many organisms, including bacteria, which form homogeneous or heterogeneous multimeric pores on target biological membranes. These proteins involve various vital functions, including cell death, immunity, and infection[1,2]. PFPs are produced as soluble monomers that form ring-shaped oligomers and subsequently create membrane-spanning α-helices or β-barrels to form pores in various biological membranes. Toxic PFPs are known as pore-forming toxins (PFTs). These PFTs can disrupt the homeostasis of target cells by forming pores, leading to the efflux of ions, amino acids, and water and ultimately inducing cell death.

Clostridium perfringens[3], Clostridioides difficile[4], Clostridium spiroforme[5], Clostridium botulinum[6] and Bacillus anthracis[7] produce binary toxins (Iota toxin; Ia and Ib, CDT; CDTa and CDTb, CST; CSTa and CSTb, C2 toxin; C2I and C2II, Anthrax toxin; LF, EF, and PA) composed of enzymatic and membrane-binding components which function as PFPs[8]. Binary toxins are classified into two groups: intestinal toxins from Clostridium, including the Iota toxin, CDT, CST, and C2 toxin, which have homologous enzyme components such as actin ADP-ribosyltransferase. The other is the anthrax toxin, whose enzyme components (EF and LF) differ from those of clostridial ADP-ribosyltransferases in both structure and function. However, the membrane-binding components of these toxins are highly conserved, except for their receptor-binding domains. The addition of the enzymatic component alone to cells or organisms does not result in activity, whereas the membrane-binding component alone induces necrosis and dermonecrosis[9,10]. However, components A and B co-addition increases toxicity compared to their individual addition, inducing morphological changes and cell death[11].

Cell entry mechanisms are similar for clostridial binary toxins and anthrax toxins. The monomeric membrane-binding component binds to the target cell receptor and is activated by proteases to form a soluble ring-shaped oligomer (prepore). The endosomes take up the enzymatic components and prepores. As the endosome acidifies, the pore undergoes a conformational change into a membrane-spanning β-barrel pore, allowing the enzymatic component to translocate into the cell[12,13]. The translocated enzymatic component exerts severe effects on host cells through actin depolymerisation via ADP-ribosylation activity by clostridial binary toxins[6,14,15], or inhibition of signalling pathways through degradation of MAPKK in anthrax toxin[16,17]. At first, it was shown that the pore of PA forms the narrowest constriction site (ϕ-clamp) with a diameter of only 6 Å in the centre[18,19]. Understanding how the enzymatic component passes through the ϕ-clamp is key interest in studying membrane translocation mechanisms of binary toxins. We previously determined the cryo-electron microscopy (cryo-EM) structures of the enzyme-pore complexes of the iota and CDT toxins[20,21]. The constriction

sites of Ib and CDTb, as named ϕ-clamp in PA, were conserved among Ib and CDTb. We found that after complex formation with Ca-edge and NSQ-loop, which are constriction-sites of the pore, the N-terminal α-helix of the enzymatic component tilts towards the ϕ-clamp, and this structure further unfolds[20,21]. In the case of anthrax toxin, the first α-helix of LF and EF unfold and dock into a deep amphipathic cleft called the α-clamp[22]. Thus, N-terminal unfolding is commonly observed in clostridial binary toxins and anthrax toxins; however, they use different modes. It is hypothesised that the disordered structure passes through the ϕ-clamp and refolds its secondary structure within the β-barrel or cytosol. As described above, binary toxin membrane pores are not only pore-forming toxins but also serve as an intriguing research subject because of their unique translocation mechanism involving the unfolding of the enzymatic component.

Mutations in the F427 residue forming the ϕ-clamp of the anthrax toxin PA-pore, as well as the surrounding residues, have significant effects on the maturation from prepore to pore and the translocation activity of the enzymatic component[23–25]. In anthrax PA, the D425A point mutation, two residues upstream of F427, does not affect the oligomerisation ability but inhibits the conformational change to the pore state. Cryo-EM structural analysis of this mutant revealed that the oligomer was formed by PA protomers in multiple intermediate states between prepore and pore conformations[26]. Furthermore, adjacent protomers have similar structural states, suggesting that maturation from prepores to pores proceeds in a domino-like manner within the heptamer. However, the complete heptamer structure of each intermediate in this domino-like pore maturation process has not yet been experimentally revealed.

We unexpectedly obtained a supercomplex in which multiple Ib oligomers were assembled radially (Ib-rosette) while preparing the wild-type Ib component of the iota toxin. A single particle structural analysis of the Ib-rosette sample revealed that it consisted of both Ib-pores with formed β-barrels and Ib-prepores without the β-barrels. A detailed analysis of the prepore class allowed us to determine the structure of a seven-fold symmetric prepore for the first time in Ib and multiple asymmetric prepore structures. Comparison with previously reported structures revealed that the protomers forming these prepores were in an intermediate state between the prepore and pore states. Furthermore, comparison of the series of obtained overall structures suggested that the symmetrically arranged protomers underwent a partial loss of symmetry, and this structural change proceeded step-by-step in a domino-like manner to mature into pores. In this paper, we report on the pore maturation process deduced from comparing multiple prepore structures and high-resolution pore structure obtained in this study.

Results

Cryo-EM single particle analysis of Ib-rosette

While attempting to prepare Ib-pores reconstituted in liposomes, the obtained sample was observed using negative staining and cryo-EM revealing that the structure consisted of multiple radially assembled Ib oligomers (referred to as Ib-rosette) **(Extended Data Fig. 1a,b)**. Focusing on the individual units of the oligomers, single particle structural analysis using CryoSPARC[27] revealed that the sample contained not only particles of Ib-pores with membrane−spanning regions covered by lipid micelles, but also particles of Ib-prepores where the β-barrel was not yet formed (**Extended Data Fig. 1c–g**). The prepore particle set could be further classified into five subclasses: particles with an open central region and particles with a constricted central structure where the base of the β-barrel has formed but is still immature. Other intermediate states between these forms **(Extended Data Fig. 2a)** suggest that the prepore particle set was composed of protomers in multiple states. Structural analysis at the protomer level for each class revealed that the heptameric prepore state is formed by three distinct protomer states, which differ from those in the pore state: the initial state, early intermediate state (early int.), and late intermediate (late int.). The structural characteristics of each state are described in the following sections **(Fig. 2)**. The particle sets for each prepore (class 1–4) were classified into eight classes with a complicated workflow **(Extended Data Fig. 2)**, reflecting the different proportions of these three states **(Fig. 1a-j).**

During the single particle analysis of the Ib-pore, multiple pore states with varying degrees of β-barrel maturation were observed. These states exhibit no distinguishing features other than the length of the β-barrel. Focusing on the particle set that formed a fully extended β-barrel, particle images were selected for map calculation **(Fig. 1k)**. Atomic models were refined against the density maps of the prepores and the pore, allowing for a comparative analysis of their structural characteristics.

Structure comparison of Ib protomers

Ib consists of four domains: D1, which binds to the enzymatic component Ia; D2, which forms the pore lumen; D3, which interacts with other domains and contributes to structural stabilisation directly; and D4, which is responsible for binding to the target cell receptor **(Fig. 2a,b)**. The most significant structural differences were observed for D2 among the obtained protomer states. D2 can be further subdivided into D2c, which serves as the structural foundation of the oligomer, and D2s, which form β-barrels upon pore formation. Structural changes were observed in both the subdomains. The visibility of the D2s density served as a key indicator for obtaining multiple prepore classes during the single particle analysis **(Extended Data Fig. 2c)**. While protomers with visible densities have D2s within them, those without visible densities have D2s in a popped-out and flexible state. The class with visible D2s can be further subdivided into two additional states based on structural changes in D2c at the protomers interface. Consequently, the prepores comprised protomers in three distinct states, except for the pore state **(Fig. 2d-i, Supplementary Movie 1)**.

The first state is where Prepore I is arranged in a sevenfold cyclic symmetric (C7) configuration, and this was termed the "initial state" **(Fig. 2d,g)**. The initial state is similar to the monomeric structural state of CDTb (PDBID:8DCM) and PA (PDBID:1ACC) reported in previous studies **(Extended Data Fig. 4)**[28,29]. The second state has a structure where β7 and β8 on the D2c domain at the protomer interface are shifted towards the CCW (counter-clockwise) protomer compared to the initial state, and this was termed the "Early intermediate state" (abbreviated as Early int.) **(Fig. 2e,h,k, Supplementary Movie 2)**. The third state is where D2s are released from the protomer and become invisible, and this was termed the "Late intermediate state" (abbreviated as Late int.) **(Fig. 2f,i)**. In the Late int., compared to the Early int., in addition to the difference in D2s visibility, the position of α5 on the D2c domain was observed to shift towards the centre of the oligomer **(Fig. 2l)**. The Late int. is quite similar to the structure of the pore (Pore state), except that the β-barrel has not yet formed, and some differences observed in the arrangement of the secondary structures. A structural comparison of the Late int. and the Pore state is described in the following section. Although the characteristic structural changes mentioned above were observed in D2c and D2s, no changes were observed in the Ca-edge and NSQ-loop, which are the binding sites for substrate Ia in each structure **(Fig. 2j)**. Based on the backbone root mean square deviation (RMSD) values and previously reported monomeric homologue structures, the series of structures was suggested to change in the order of Initial state, Early int., Late int., and Pore state **(Supplementary Movie 1)**.

The arrangements of the three types of protomers that constituted the prepores obtained in this analysis were distinctive. From Prepores I to VIII, the number of protomers in the Initial state decreased by one, whereas the number of protomers in the Late int. increased by one. In addition, Late int. protomers were not scattered throughout the oligomer but were adjacent to each other **(Fig.1a-h, Extended Data Fig. 5)**. This structural feature suggests the possibility of a step-by-step conformational change from a heptameric prepore to a pore structure in a domino-like manner, temporarily losing its symmetry. Another notable feature is that there was always one Early int. in the CCW direction from a Late int. These observations suggest two possible models: the CCW model, in which Early int. served as the starting point for the conformational change, with a Late int. increasing one by one in the CCW direction, and the CW (clockwise) model, where the Late int. induced a conformational change in the adjacent protomer in the CW direction, converting it from its Initial state to an Early int.

Conformational change at the protomers interface

It was necessary to consider the influence of the structural changes of each protomer on adjacent protomers to interpret the step-by-step conformational changes. Therefore, structural comparisons were made in pairs of protomers. In the Initial state-Initial state interface, which is considered to represent the earliest structure, the structure around β7-8 showed a gap between the CCW protomer. In contrast, at the Early int.-Late int. interface, the structure was tightly zipped, increasing the varied surface area of the interface **(Fig. 3a-d, Supplementary Movie 2)**. In other words, the initial structural changes between the protomers can be considered a process of reducing the solvent-exposed surface area and gaining interactions between the protomer pairs.

Next, the structural changes in the Early int.-Late int. interface and Late int.-Late int. interface were examined. However, as described above, no significant structural changes were observed at these interfaces. In contrast, Prepore VIII was found to have a relatively constricted structure with a more densely filled central density than earlier prepores **(Fig. 3e-h, Extended Data Fig. 6)**. This suggests that during the conformational change from the prepore to the pore state, the residues forming the constriction-site, known as the ϕ-clamp, gradually converged towards the centre. Since the residues forming the ϕ-clamp are located near α5 (aa. 460-473), it is expected that this is linked to the shift of α5 observed during the transition from Early int. to Late int. **(Fig. 2l, Supplementary Movie 1,3)**. In summary, these features suggest a conformational change from the Early int. to Late int. represents a preliminary step in forming the constriction-site at the centre of the oligomer, which is facilitated by the steps mentioned

above. Notably, in the structure of Prepore VIII, a clear density for the ϕ-clamp and the surrounding residues (aa. 451-458) was not observed, indicating that a stable constriction-site, as seen in the Pore state, had not yet formed.

High-resolution structure of Ib-pore

We previously reported the structures of Ib-pores solubilised with LMNG and the Ia-bound Ib-pore complex[20]. In this analysis, the resolution of the Ib-pore was further improved, and a clear density was obtained up to the tip of the β-barrel compared with previous analyses **(Fig. 4a,b)**. The Ib-pore contains several distinct constriction-sites within its lumen **(Fig. 4c)**. As described in the previous section, the Ca-edge and the NSQ-loop, which are involved in binding to the enzymatic component, did not undergo structural changes from the prepore to the pore **(Fig.2c)**. The most significantly changed constriction-site was the ϕ-clamp, which was not observed in Prepore I, showed unclear density in Prepore VIII, and was observed in Ib-pore **(Extended Data Fig.6, Fig. 3e-h, Fig. 4d)**.

In the density measurements obtained at the tip of the β–barrel, the hydroxyl groups of Y356 and Y344 were oriented outwards from the TM region, showing the characteristic snorkelling effect of transmembrane proteins. The amino acid side chains oriented inward in the β-barrel are rich in Ser/Thr and are relatively small. The side chain density of Q345, located at the hairpin turn of the β-barrel, extended towards the centre, indicating constriction **(Fig. 4c,e)**. However, the side chain density was relatively unclear and the side chains were far from each other, which suggested that the structure was flexible. Furthermore, in the Pore state, α5 was shown to shift towards the base of the β-barrel from Prepore VIII, forming interactions and stabilising the structure **(Fig. 4f,g)**. As observed in the structural transitions from Early int. to Late int. and from Late int. to the Pore state, the formation of the ϕ-clamp (F454) and the shift of α5 (aa. 460-473) appear to be linked.

Discussion

This study, utilising cryo-EM analysis, revealed the step-by-step conformational changes in bacterial PFTs as they transitioned from soluble prepores to membrane-spanning pores. Although the general mode of action of PFTs is widely recognised, detailed insights into their structural changes have mostly been based on comparisons of a few stable states and biochemical experiments with mutants. We uncovered multiple structures, including intermediates during pore formation **(Fig. 1)**: the early immature state of soluble monomers forming a symmetric oligomer (Prepore I), asymmetric oligomers with structural changes in some protomers (Prepore II-VII), the fully matured symmetric Prepore VIII, and the membrane translocating the β-barrel in the pore. These comparisons improve our understanding of structural changes within individual protomers and allow for a more thorough discussion of the overall maturation process of binary toxin pores.

In our previous cryo-EM study of the Iota toxin, we determined the structures of both the Ib-pore and the Ia-bound Ib-pore complex (as well as the CDTa-bound CDTb-pore complex), revealing the docking mode of the enzymatic component as the initial step of its translocation through the Ib-pore, and showed that the N-terminus undergoes unfolding[20,21]. The results of this study revealed the detailed structures of the earlier steps, enabling a more comprehensive understanding of the cellular entry mechanisms of binary toxins. Scott et al. also reported, using cryo-EM analysis of the D425A mutant of the anthrax toxin PA (which inhibits pore formation), which is based on the appearance of the density map of the receptor-binding domain, that the structural variety among PA protomers within the oligomer was classified into distinct states. Moreover, protomers with similar structural states tend to be adjacent to each other within oligomer[26]. This study classified various protomer states based on their structural features on D2c and D2s using cryo-EM analysis and wild-type *Clostridium perfringens* iota toxin Ib samples. In addition, multiple structural states of the entire oligomer were successfully identified. Finally, we identified the characteristic structural changes in the protomers and classified them into four states: Initial state, Early int., Late int., and Pore state. Furthermore, these protomer states were distributed in a distinctive pattern, in which the Late int. are always adjacent to each other at Early int. was positioned in the most CW direction within the oligomer, suggesting a regularity in the structural transition process **(Fig. 1a-h)**.

Initially, we aimed to prepare the Ib-pores in a lipid membrane environment using liposomes for solubilisation. However, the particles obtained were not proteoliposomes but rather aggregates of Ib oligomers assembled radially **(Extended Data Fig. 1a)**. Similar aggregates have been observed in the oligomers of the anthrax toxin PA, another binary toxin. It

has been reported that such structures can be obtained by incubating oligomers bound to a carrier under acidic conditions[30] (However, unlike this study, structural analysis of the constituent oligomers has not been achieved). Our previous study found that Ib oligomers dispersed in solution did not form aggregates when incubated under acidic conditions but instead underwent dramatic aggregation[20]. Considering their similarities to previous studies, it is likely that these structures form when aggregation occurs under conditions in which the mobility of the oligomers is restricted. The antigen component of the influenza virus vaccine forms a radial structure composed of HA proteins referred to as the HA rosette[31,32]. Following this convention, we refer to the aggregated Ib structure as the Ib-rosette.

The Ib-rosette is an aggregate composed of multiple Ib oligomers; however, single particle structural analysis is possible by focusing on each oligomer. During the analysis, it was found that these oligomers included prepore structures without β-barrels, partially formed β-barrels, and fully formed β-barrel **(Extended Data Fig. 1c–g)**. When observing the two-dimensional average images of the prepore class, an ambiguous density was found in the side view, in the direction where the β-barrel would form **(Extended Data Fig. 1f,g)**. This indicated that other oligomers might spatially hinder the formation of the β-barrel. In CDTb, it is known that paired heptamers form a dimer of heptamers; however, clear two-dimensional images of each heptamer are observed in these cases. The average images of this Ib-prepore class are considered to be different[33,34]. We performed a more detailed classification of the prepore classes, and obtained high-resolution density maps for each of the eight prepores and pore **(Extended Data Fig. 2)**. Notably, classification based on the differences in the structural states of each protomer revealed that both asymmetric and symmetric prepore states existed **(Fig. 1)**.

Prepore I was composed of the Initial state, in which the D2s region was stored within the protomer, arranged in a seven-fold symmetrical manner **(Fig. 1a)**. The initial state has a structure highly homologous to previously reported PA monomers and CDTb monomers and is considered to be an early stage in the alignment of soluble protomers in the initial phase of maturation **(Extended Data Fig. 4)**. The Early int. observed in Prepore II-VII is a state in which β7-8 has shifted towards the adjacent protomer in the CCW direction, suggesting that this partial structure is in a transition **(Fig. 2k, Fig. 3a-d, Supplementary Movie 2)**. Notably, Early int. is always positioned in the CW direction relative to Late int. except for Prepore VII, and was never observed in the CCW direction. Furthermore, Late int. appeared consecutively. Based on these observations, we propose two possible models: (1) A CCW model in which the Early int. stabilises the adjacent protomer on the CCW side into Late int., which stabilise Late int. further induces the stabilisation of the next protomer on the CCW side into the Late int. state. (2) A CW

308 model in which Early int. matures into the Late int, stabilising the Initial state protomer on the
309 CW side into the Early int. state, and this process continues sequentially. Structural changes
310 within a series of protomers should not occur simultaneously but rather in a stepwise manner. In
311 other words, it is unlikely that an Initial state will abruptly convert into a Late state, as observed
312 in the CCW model. In this context, we consider the CW model, where each protomer gradually
313 converts from an Initial state to an Early int. and then to a Late int., as a more plausible
314 explanation **(Supplementary Movie 3)**. In both models, the early stage of maturation from
315 Prepore I involved forming a pair of Early ints. and Late int. compared to the adjacent Initial
316 state. These findings suggest that a series of structural changes occurred step-by-step and
317 domino-like manner.
318
319
320 Upon examining the entire oligomer structure, the central radius is observed to
321 progressively narrow during the maturation from prepore to pore, with the most constricted
322 region having a diameter of only 6 Å **(Fig. 4c,d)**. A conserved phenylalanine residue across
323 various binary toxin pores forms this constricted region. Mutational studies using PA have
324 revealed that this residue is crucial for pore formation activity[24]. The F454 residue of Ib is
325 located upstream of α5 (aa. 460-473), which undergoes the most significant structural shift
326 during the transition from Early int. to Late int. The density of the residues surrounding F454
327 (aa. 449-460) was not observed in the Initial state or Early int., suggesting that these residues
328 possessed a flexible structure **(Fig. 3f)**. In the Late int., the density became more apparent,
329 especially in Prepore VIII, where the main-chain structure could be roughly traced. This
330 observation indicates that the constricted region gradually forms during the transition to the late
331 int. **(Fig. 3h)**. No significant structural changes were observed in the Early int.-Late int.
332 interface or the Late-Late int interface, suggesting that the partial formation of the constricted
333 region, accompanied by the shift of α5, may lead to the tendency for adjacent Late int. to
334 associate. The most distinctive difference between the Prepore VIII and Pore structures is the
335 presence or absence of β-barrel formation. In Prepore VIII, the F454 density was ambiguous,
336 but it was clear in the Pore state, indicating the formation of a stable ϕ-clamp. During this
337 process between Prepore VIII and Pore, the further shift of α5 forms interactions with the base
338 of D2s, stabilising the β-barrel foundation **(Fig. 4f,g)**. Scott *et al.* reported that the D425 mutant
339 of anthrax PA, which is adjacent to F427 and responsible for forming the ϕ-clamp, inhibited
340 pore formation[26]. This residue faces inward within the ϕ-clamp loop, forming hydrogen bonds
341 stabilising the constriction-site. In Ib, D452 forms a bond with R457, binding to the P460 main-
342 chain near α5 (aa. 460-473). This interaction suggests that the proper formation of the

343 constriction-site is closely related to the movement of α5 and may also be linked to the
344 formation of the β-barrel.
345
346 The enzymatic components believed to pass through the pores exhibit different
347 stoichiometries and binding positions in the iota toxin and anthrax toxins. In anthrax toxin, three
348 enzyme molecules, LF and EF, bind to a single pore, with their N-terminal α-helices interacting
349 with the α-clamp formed at the interface of PA protomers[35–37]. In contrast, the single enzymatic
350 components of the iota toxin and CDT bind to the Ca-edge of the pore, with its N-terminal helix
351 unfolding at the NSQ-loop[20,21]. For binary toxin pores with a narrow constriction such as ϕ-
352 clamp, the docking and unfolding of the enzymatic component from the Ca-edge to the NSQ-
353 loop represent critical steps for activity. Notably, these regions remain unchanged in the
354 structures of the individual monomers reported in this study **(Fig. 2j)**. This suggests that the
355 enzymatic component can bind to the oligomer in both immature and mature states. In addition,
356 the high-resolution cryo-EM density of the pore structure reported in this study revealed a
357 constriction formed by Q345 at the tip of the β-barrel, which served as the exit for membrane
358 translocation **(Fig. 4c,e)**. The diameter of this constriction site is less than 10 Å, which is
359 smaller than the general diameter of an α-helix. Although a clear density was observed in the ϕ-
360 clamp, the density of this constriction was low, suggesting that it was relatively unstable.
361 Additionally, this residue is neither sequenced nor structurally conserved in the PA pore,
362 making it unlikely to pose steric hindrance to membrane translocation. However, the side chain
363 of Q345, located towards the centre, may weakly interact with individual residues of Ia ongoing
364 membrane translocation, indicating that this residue should be considered in future
365 investigations as a key residue that may modulate the translocation process.
366

367 This study has enabled the discussion of the maturation process from Prepore to Pore in binary
368 toxins at the molecular structural level, supported by the cryo-EM density **(Fig. 5)**. However, it
369 should be noted that the observation of these structural states may have been made possible by
370 the formation of the Ib-rosette, which potentially sterically hindered pore formation. Therefore,
371 it is necessary to consider the possibility that the obtained structures may be artefacts, similar to
372 samples in which pore maturation was cancelled by introducing mutations. However, the
373 formation of the Ib-rosette may have enabled the trapping of unstable intermediates that also
374 occurred during the normal transition from the prepore to the pore. Based on a comparison of
375 the obtained structures, we proposed two models of structural change: CW and CCW. We
376 considered the CW model the most plausible, as described above. Jiao *et al.* concluded that
377 perforin undergoes a CW structural change by comparing temporal observations of the same

378 molecule using atomic force microscopy (AFM) and specific directional structural perturbations
379 through MD simulations[38]. In contrast, the semi-stable structural states determined via cryo-EM
380 are outputs averaged from multiple and individual particle images, making it impossible to
381 correspond to the protomers between states definitively. During the maturation of the prepore,
382 the number of Late ints. protomers increased sequentially. However, whether this structural
383 change proceeds via Early int. or directly from the Initial state, corresponding to the CW and
384 CCW models, respectively, remains to be investigated. In addition, the domino-like structural
385 change in the prepore progressed through forming a pair of Early int. and Late int. as observed
386 during the transition from Prepore I to Prepore II. However, it is also possible that the
387 maturation process proceeds from more than two initiation points or occurs before heptamer
388 formation. This hypothesis needs to be discussed, considering the speed of the maturation
389 process and the likelihood of the emergence of additional initiation points. Future experiments
390 involving single-molecule observations or simulations are expected to address these challenges
391 and elucidate the detailed mechanisms of pore maturation.

392

393 PFPs are major components of bacterial toxins and the immune system and have
394 become intriguing targets in both fundamental research and applications, such as their use as
395 nanodevices in nanopore sequencing. However, these complicated proteins are produced as
396 soluble monomers that mature into functional pores through dynamic structural changes. Binary
397 toxins possess unique characteristics among pore-forming toxins that enable the translocation of
398 enzymatic components into target cells via pores, making them highly applicable. Research is
399 being conducted to create carriers by conjugating proteins to the binding domain of the
400 enzymatic component, facilitating the intracellular delivery of the desired molecules[24,39]. In this
401 study, we report multiple structural states during the pore-forming process of a binary toxin that
402 was previously difficult to obtain, through detailed classification using cryo-EM. We expect that
403 the findings of this study will facilitate our understanding of the maturation processes of PFPs in
404 general and contribute to the advancement of nanodevice development based on this structural
405 foundation.
406
407

408 **Methods**

409 **Expression and purification of Ib**

410 Ib was expressed with a 20 kDa pro-sequence at the N-terminus, which inhibits
411 oligomer formation, and a 6-His tag at the C-terminus. Specifically, the gene encoding Ib
412 (Uniprot ID: Q46221, residues 40-875) was cloned into pET23a without the signal sequence or
413 other tags. The plasmid was transformed into *Escherichia coli* BL21 (DE3) and cultured in LB
414 medium containing 50 ng/μl ampicillin at 37°C. When the culture reached an OD600 of 0.6,
415 IPTG was added to a final concentration of 1 mM, and the culture was incubated for an
416 additional 16 hours at 23°C. The cells were harvested by centrifugation.
417

418 The harvested cells were resuspended in buffer A (20 mM Tris pH 8.0, 100 mM NaCl, 1.0 mM
419 CaCl2, 20 mM imidazole) containing one complete ULTRA Tablet (Roche, Basel, Switzerland)
420 and lysed by sonication on ice. The lysate was subjected to ultracentrifugation (180,000*g*, 40
421 min) and the soluble fraction was bound to a Ni-NTA column. The column was washed with 10
422 volumes of buffer A and eluted with buffer B (20 mM Tris, pH 8.0, 100 mM NaCl, 1.0 mM
423 CaCl2, and 500 mM imidazole). The eluate was concentrated by centrifugation using a 50 K
424 ultrafiltration membrane and exchanged with buffer C (20 mM Tris, pH 8.0, 100 mM NaCl, 1.0
425 mM CaCl2).

426

427 **Sample preparation of Ib-rosette**

428 Ib was activated and oligomerised in our previous studies[6]. Monomeric Ib was
429 incubated at room temperature for 1 h with chymotrypsin at a 1/1,000 mass ratio. The reaction
430 was stopped by adding PMSF (phenylmethylsulfonyl fluoride) at a final concentration of 1 mM
431 to inhibit chymotrypsin activity. Ethanol was then added to a final concentration of 10% (v/v),
432 and the mixture was incubated at 37°C for 1 h to promote Ib oligomerisation. 450 μl of the Ib
433 oligomer solution was added to a Ni-NTA resin and washed with buffer C to remove ethanol.
434 540 μl of prepared liposomes (made by drying E. coli Extract Polar (Sigma-Aldrich) under N2
435 gas, resuspending with Buffer C, and processing through an extruder (Sigma-Aldrich) with a
436 100 nm filter), 360 μl of buffer C, and 100 μl of 1 M MES (pH 5.5) were then added, followed
437 by incubation at 4°C for 16 hours. The resin was washed with ten column volumes of buffer A
438 and eluted with buffer B. The eluted product was subjected to gel filtration using HiLoadTM
439 16/200 SuperdexTM 200pg of buffer C at a flow rate of 0.8 mg/ml. Fractions containing the Ib
440 oligomer bands were collected based on SDS-PAGE observation and concentrated to 1.0 mg/ml
441 using a 50 K ultrafiltration membrane.
442

Data collection with Cryo-EM

The prepared sample (3 µl) was applied to hydrophilised Quantifoil R1.2/1.3, 300 mesh (Cu), and blotted for 7 seconds using a Vitrobot Mark IV (Thermo Fisher Scientific), followed by rapid freezing in liquid ethane. The frozen grids were imaged using Glacios (Thermo Fisher Scientific) equipped with a Falcon4 direct electron detector at the Institute for Life and Medical Sciences at Kyoto University to screen the grid preparation conditions through single-particle analysis. The final data were collected using a Titan Krios (Thermo Fisher Scientific) equipped with a K3 direct electron detector (Gatan), a BioQuantum energy filter (Gatan) with a slit width of 20 eV, and a Cs corrector (CEOS, GmbH) at the Institute for Protein Research, Osaka University, with a pixel size of 0.88 Å/pix, capturing 11,549 micrographs. The detailed imaging conditions are listed in Table 1.

Single particle analysis of Ib-pore

A series of analyses of the cryo-EM images was conducted using CryoSPARC (ver.3.3.2.)[27]. Motion correction was performed using Patch Motion Correction, and CTF estimation was performed using Patch CTF Estimation. Particle images were obtained using a Template Picker with a reference created by back-projecting a previously reported Ib-pore density map (EMD-0721). The particle images were extracted and downscaled to 1/4 of their original size. These extracted particles were roughly classified through Heterogeneous Refinement with C7 symmetry applied, resulting in a distinction between the prepore class, which lacks a β-barrel, and the pore class which has a β-barrel. The detailed analysis of the prepore class is described later in the "Classification of Ib-prepore" section, where the classification procedure is outlined. More homologous particle images were selected for the pore class through 3D Variability Analysis (3DVA)[40] and no-align 3D classification. The resulting particle set was re-extracted without rescaling, and a 3D density map was reconstructed using Homogeneous Refinement. Additionally, Local Motion Correction[41] was performed to correct for per-particle motion, followed by Homogeneous Refinement of images with defocus correction[42]. The local resolution was estimated with the RELION[43] Local Resolution job

Classification of Ib-prepore

3DVA was performed on the prepore class, resulting in the classification of circular oligomers into five distinct subclasses ranging from an expanded state to a more constricted state **(Extended Data Fig.2a)**. Class 5, the most constricted class, exhibited a structure partially forming a β-barrel, similar to the pore state; thus, further analysis was not conducted for this class. The remaining classes 1-4 were subjected to Symmetry Expansion with C7 symmetry,

where the particle images were symmetrically replicated seven times. A mask was created focusing on one protomer, and the 3DVA of the protomer was used to distinguish between classes with and without an observable density corresponding to the D2s within the protomer (**Extended Data Fig. 2b,c**). For Classes 1 and 2, the maps were reconstructed using Homogeneous Reconstruction only with the particle sets where D2s were not visible, whereas Classes 3 and 4 used particle sets where D2s were visible. These reconstructions were references for refining the original particle sets before replication using nonuniform refinement. Among the resulting density maps, protomers, where D2s were ambiguously visible, were subjected to focused non-aligned 3D classification to separate classes where D2s were visible from those where they were not; this process was iteratively repeated (**Extended Data Fig. 2e–g**). Ultimately, the prepore states were classified into eight distinct classes, each differing in the number of protomers with clearly visible D2s. Finally, Non-uniform Refinement[44] and Local refinement were performed for each of the eight prepore classes. The local resolution was estimated with the RELION[43] Local Resolution job

Model building

As structures such as the initial state and early int., where D2s are folded within the protomer, have not been previously reported in Ib, the predicted models were used as the initial model. The structure predicted from the Alphafold Database was edited to start the residue numbering from 1 after the signal sequence based on the amino acid sequence of Ib (Uniplot ID: Q46221), and used as the initial atomic model for the initial state. The predicted model was fitted as a rigid body into the most clearly observed initial state density in the Prepore I map using UCSF ChimeraX (ver.1.2.4)[45], followed by manual model refinement using Coot (ver.0.9.5)[46] and automated structural refinement using PHENIX (ver.1.19.2)[47]. For Early int., the refined initial state was used as the starting model. In contrast, for late int. and the pore state, the known Ib-pore structure (PDBID:6KLW) was used as the starting model and refinement was conducted against the respective density maps of Prepore II–VIII, and Pore in the same manner as described above. Although the D4-I structure of Ib, including its pore structure, has not been previously reported, its density was observed in Prepore I. Therefore, the refined D4-I structure from Prepore I was used as the initial model for other oligomers and structural refinement was conducted again using PHENIX. Finally, the chain orientations were validated using MolProbity[48] for the models obtained using the above process. Inner radius of Ib-pore was calculated using HOLE2[49] software.

Data availability statement

The Cryo-EM maps and coordinates were deposited to the Electron Microscopy Data Bank (EMDB) and Protein Data Bank (PDB) with the accession codes EMD-61772 and PDBID 9JSG for Pore state, EMD-61771 and PDBID 9JSF for Prepore I, EMD-61774 and PDBID 9JSI for Prepore VII, EMD-61773 and PDBID 9JSH for Prepore III, EMD-61775 and PDBID 9JSK for Prepore IV, EMD-61776 and PDBID 9JSL for Prepore V, EMD-61777 and PDBID 9JSM for Prepore VI, EMD-61778 and PDBID 9JSN for Prepore VII, and EMD-61779 and PDBID 9JSO for Prepore VIII. The cryo-EM images are deposited to Electron Microscopy Public Image Analysis (EMPIAR) with the accession code XXXXXX (under depositing).

Acknowledgements

This work was supported by JSPS KAKENHI Grant Numbers 21H02452 (to H.T.), 24K01993 (to H.T.), and 21J13410 (to T.Y). This research was partially supported by the Platform Project for Supporting Drug Discovery and Life Science Research (Basis for Supporting Innovative Drug Discovery and Life Science Research (BINDS)) from AMED under Grant Number 2366 and the Joint Usage/Research Center Program of the Institute for Life and Medical Sciences at Kyoto University (to H.Y., Y.S., and T.N.). We thank J. Kishikawa, M. Hirose, and T. Kato at the Institution for Protein Research, Osaka University, for training on the techniques used for the cryo-EM study. We would like to thank Editage (www.editage.jp) for English language editing

Author contribution

All author participated in research design; T.Yamada prepared the Ib-rosette sample for cryo-EM; T.Yamada, Y.S and T.N performed cryo-EM data collection, and T.Yamada and Y.S performed single particle analysis; T.Yamada and T.Yoshida performed the atomic model building; all authors contributed to the discussion and writing the manuscript, and H.T supervised the project.

Author information

Competing interests: The authors declare no competing interests.

544 **Figure and figure legends**

545

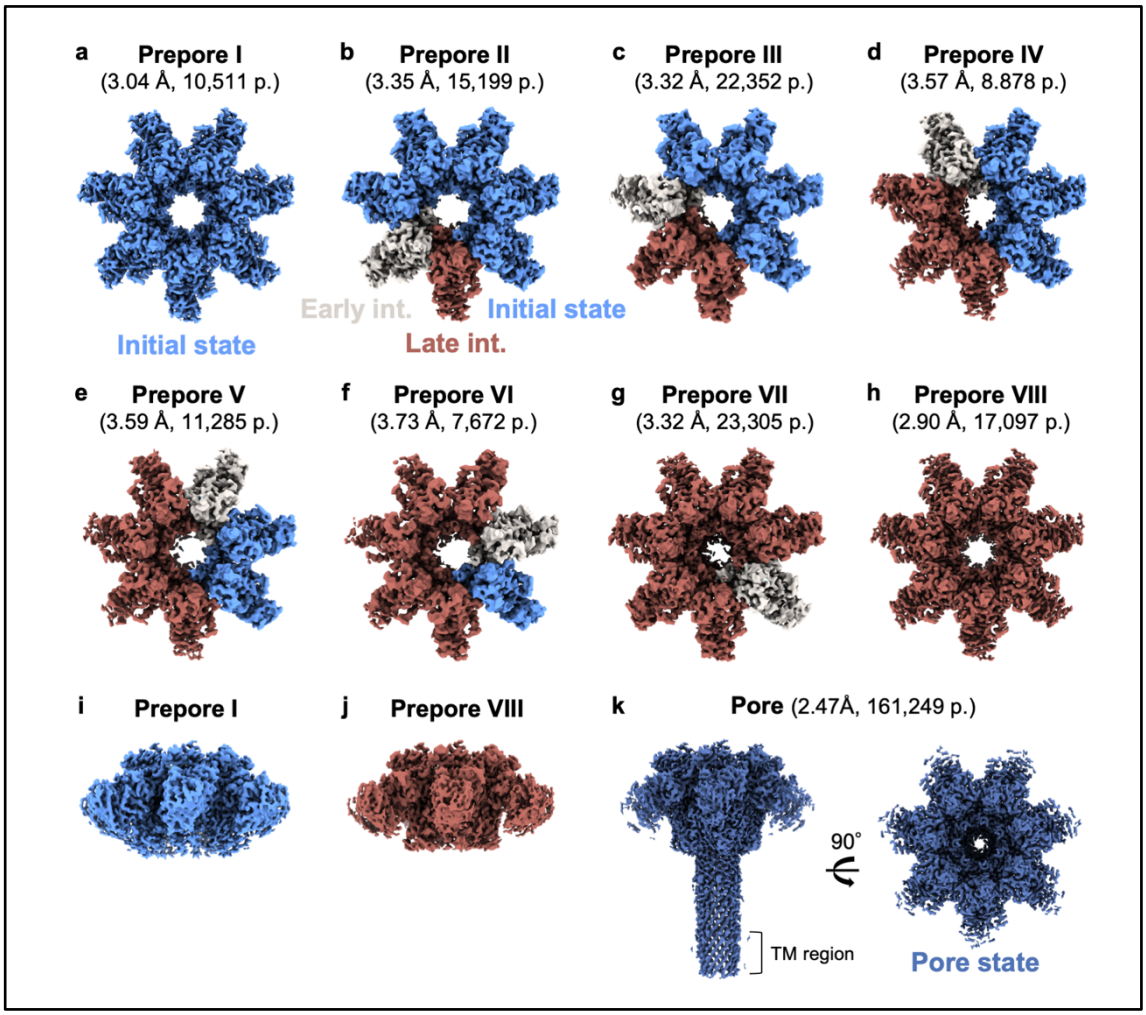

546

547 **Figure 1 | Cryo-EM maps obtained from Ib-rosette analysis**

548 **a-j** Cryo-EM maps of Ib-prepores obtained from cryo-EM single-particle analysis. **a-h** are
549 views from the top of the prepore where the enzymatic component Ia docks. **i,j** Side views of
550 Prepore I and Prepore VIII indicate that the membrane-spanning-barrel has not yet formed at
551 these stages. **k** Cryo-EM map of Ib-pore viewed from the side (left) and top (right).

552

553

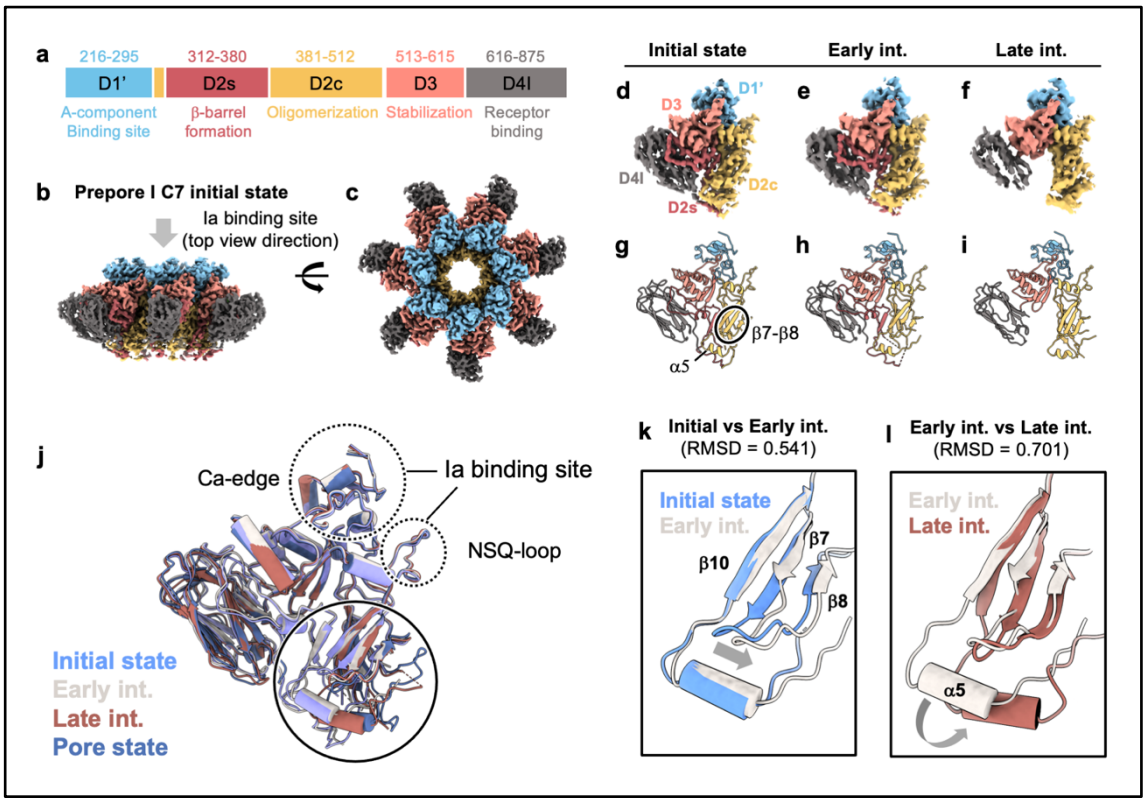

Figure 2 | Structures of Ib protomer

a Schematic of the N-terminal cleaved Ib domains with densities observed in cryo-EM maps. **b, c** Cryo-EM maps of Prepore I, coloured according to the domains shown in panel **a**. **d-i** Maps and atomic models of the Ib protomer, coloured according to the domains. The Initial state map was extracted from the Prepore I, Early int. from Prepore II, and the Late int. in Prepore VIII. **j** Atomic models of the Initial state from Prepore I, Early int. from Prepore II, Late int. from Prepore VIII, and Pore state from Pore were aligned. **k, l** Comparison of cartoon models with tube α-helix between the Initial state (cyan) vs. Early int. (white), and Early int. vs. Late int. (brown). The RMSD values were calculated using UCSF Chimerax[45].

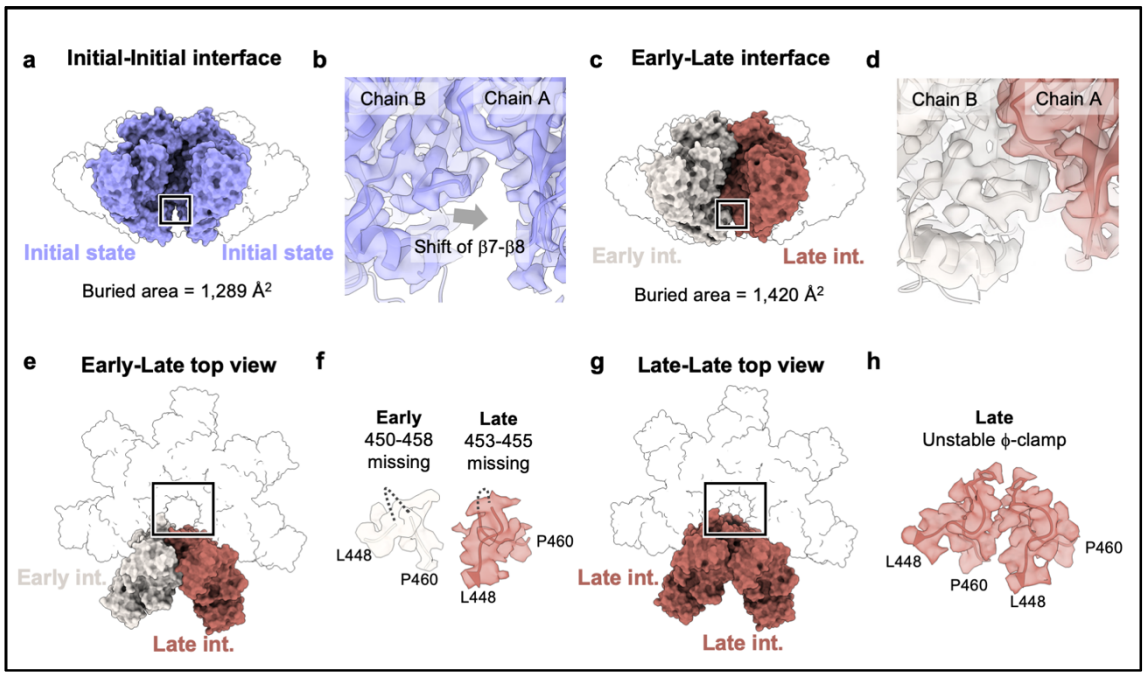

Figure 3 | Comparison of inter-protomer interactions

a-d Comparison of interface structures between the Initial state and the Initial state (Prepore I) and the interface structure between the Early int. and Late int. (Prepore II). **a,c** Surface models of interest calculated from atomic models of Prepore I and Prepore II. **b,d** Atomic models in respective cryo-EM density maps. **e-h** Comparison of constriction-site structures between the Early int. and Late int. (Prepore II) and the interface structure between the Late int. state and Late int. (Prepore VIII). **e,g** Surface models of interest calculated from the atomic models of Prepores II and VIII. **f,h** Diagram of the atomic model in the ϕ-clamp map, generated with residues 448–460, and the density map trimmed around the atoms.

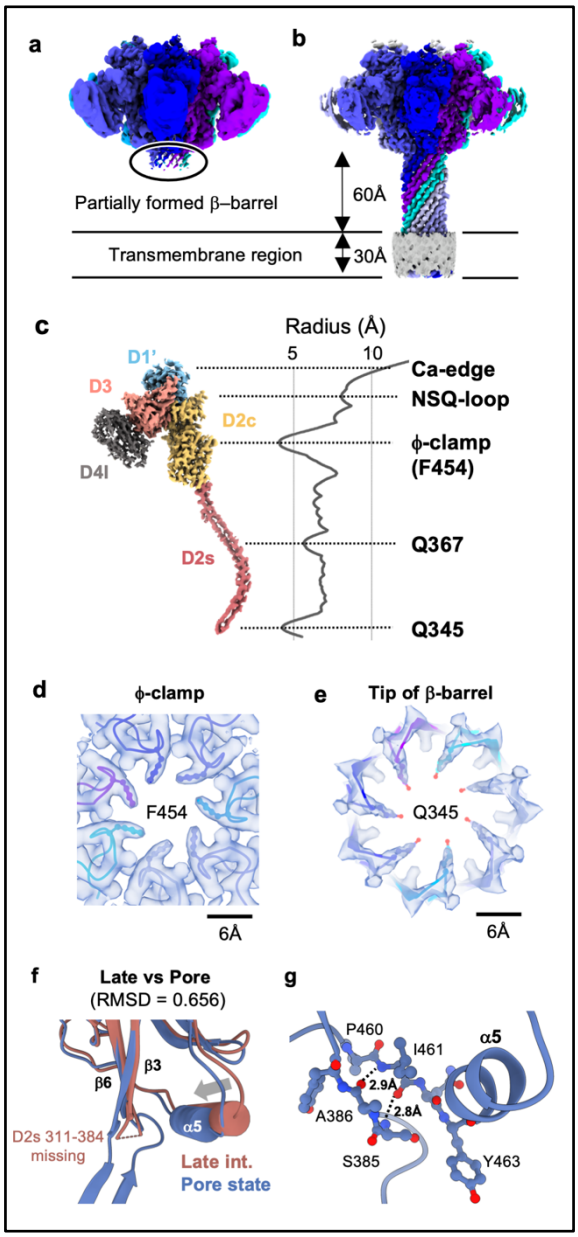

Figure 4 | Structure of Ib-pore

a,b Cryo-EM maps of Ib-pores with immature-barrel (see Extended Data Fig.2a) and fully formed-barrel. The maps are coloured according to the protomers. **c** Cryo-EM map of an Ib protomer extracted from the Ib-pore with a fully formed barrel. The inner radius was calculated using HOLE2[49] software. The positions of the constriction sites in the Ib-pore are marked with dotted lines. **d,e** Diagrams of the model showing the smallest inner radius. **f** Comparison of cartoons between Late int (brown) and the Pore state (purple). **g** Atomic model of Pore state Ib.

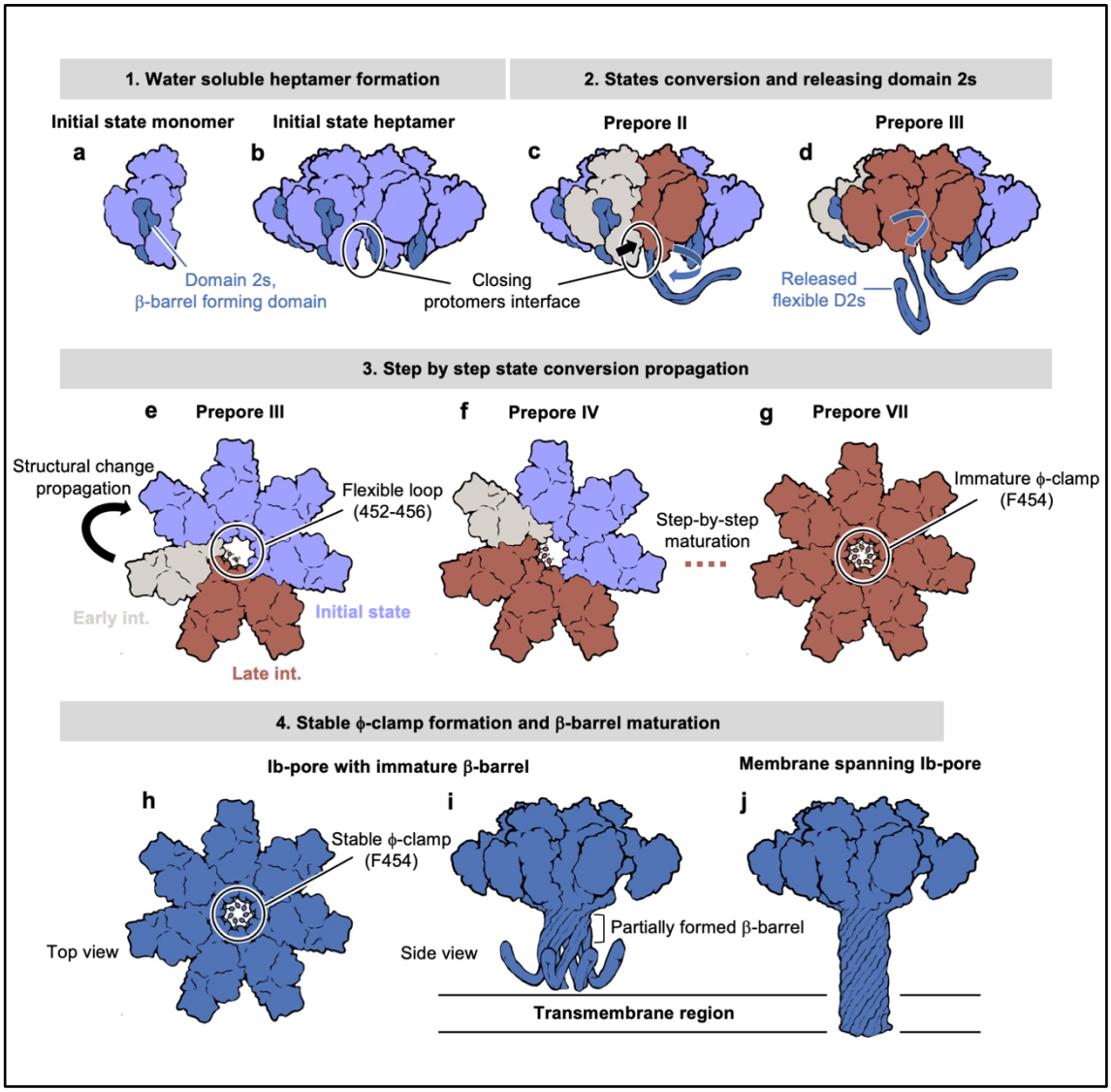

Figure 5 | Summary of Ib-pore maturation mechanism

a N-terminal cleaved active Ib monomer in its Initial state. **b** Active Ib monomers assemble into heptameric Prepore I. **c** Two adjacent protomers convert into a pair of Early int. (white), and Late int. (Red) (Prepore II). **d** Another adjacent protomer changes its state to Early int. (white), and Prepore II transitions to Prepore III, composed of four Initial state protomers, one Early int. protomer and two Late int. protomers. **e-g** Top views of the respective Ib-prepores. Number of Initial states and Late int. changed with step-by-step domino-like manner propagation. **g** The central constriction-site of the Ib-prepore is not yet fully formed but remains flexible. **h-j** Structures of the Ib-pores **h** Upon maturation to the pore, a stable ϕ-clamp is formed at the central constriction-site. The extension of the long β-barrel was achieved through the partial formation of the β-barrel from the foundation of the oligomer.

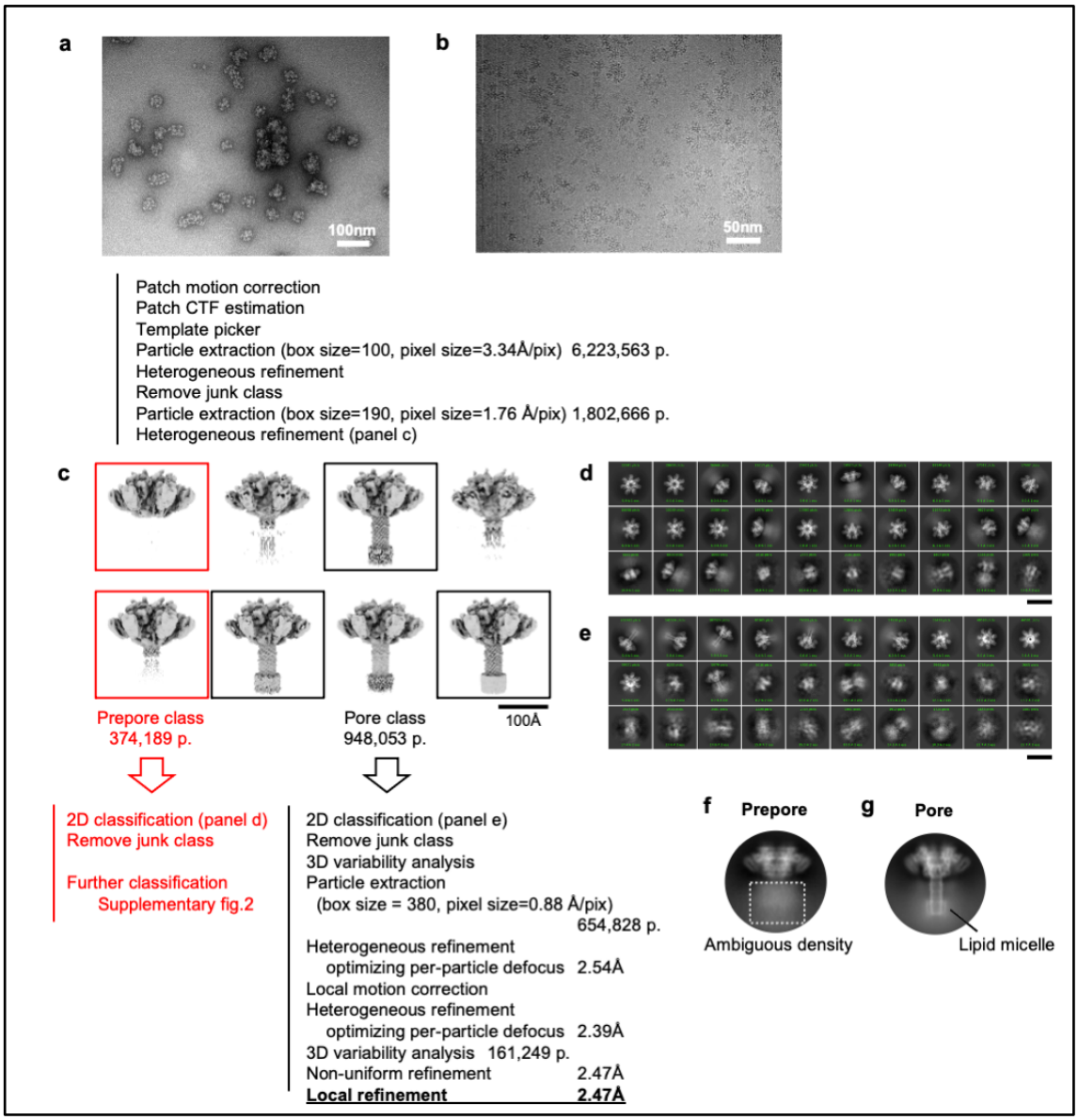

Extended Data Figure 1 | Single particle analysis workflow

a Micrograph of negatively stained Ib-rosette. **b** Cryo-EM micrograph of the Ib-rosette. **c** Representative density maps calculated using heterogeneous refinement. The classes marked with squares were manually sorted into the Ib-prepore particle set (red) and Ib-pore particle set (black). **d,e** Averaged images of Ib-prepores and Ib-pores calculated using 2D classification. The scale bar represents a length of 200 Å. **f,g** Representative 2D average images of the side views of the Ib-prepores and Ib-pores.

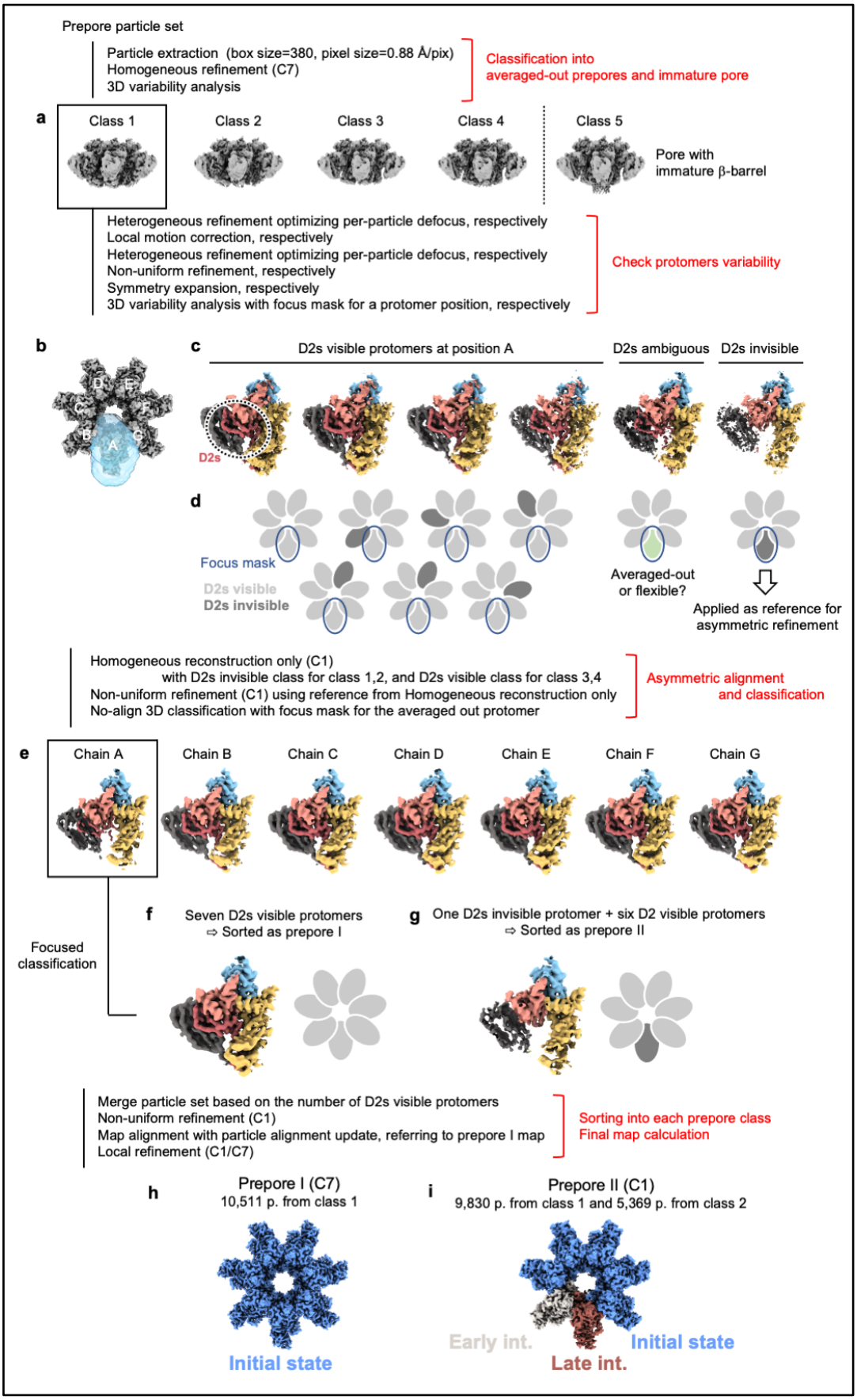
Prepore particle set
Particle extraction (box size=380, pixel size=0.88 Å/pix)
Homogeneous refinement (C7)
3D variability analysis
Classification into
averaged-out prepores and immature pore
a
Class 1
Class 2
Class 3
Class 4
Class 5
Pore with
immature β-barrel
Heterogeneous refinement optimizing per-particle defocus, respectively
Local motion correction, respectively
Heterogeneous refinement optimizing per-particle defocus, respectively
Non-uniform refinement, respectively
Symmetry expansion, respectively
3D variability analysis with focus mask for a protomer position, respectively
Check protomers variability
b
c
D2s visible protomers at position A
D2s ambiguous
D2s invisible
D2s
d
Focus mask
D2s visible
D2s invisible
Averaged-out
or flexible?
Applied as reference for
asymmetric refinement
Homogeneous reconstruction only (C1)
with D2s invisible class for class 1,2, and D2s visible class for class 3,4
Non-uniform refinement (C1) using reference from Homogeneous reconstruction only
No-align 3D classification with focus mask for the averaged out protomer
Asymmetric alignment
and classification
e
Chain A
Chain B
Chain C
Chain D
Chain E
Chain F
Chain G
Focused
classification
f
Seven D2s visible protomers
⇨ Sorted as prepore I
g
One D2s invisible protomer + six D2 visible protomers
⇨ Sorted as prepore II
Merge particle set based on the number of D2s visible protomers
Non-uniform refinement (C1)
Map alignment with particle alignment update, referring to prepore I map
Local refinement (C1/C7)
Sorting into each prepore class
Final map calculation
h
Prepore I (C7)
10,511 p. from class 1
i
Prepore II (C1)
9,830 p. from class 1 and 5,369 p. from class 2
Initial state
Early int.
Initial state
Late int.

Extended Data Figure 2 | Detailed classification workflow for Ib-prepore

a Classes obtained from 3D variability analysis. **b** Density of subunit A (transparent light blue) indicates the mask used for focused classification of symmetry-expanded particles. **c,d** Classes obtained from focused 3D variability analysis and the corresponding diagram of the possible relative positions between the focused mask and D2s-visible or D2s-invisible protomers. **e** Protomer maps extracted from the non-uniform refinement output. Subunit A shows a weak D2s density because the D2s-visible protomer (**f**) and the D2s-invisible protomer (**g**) are aligned at the same position. **h,i** Ib-prepore maps obtained from Class 1 particles.

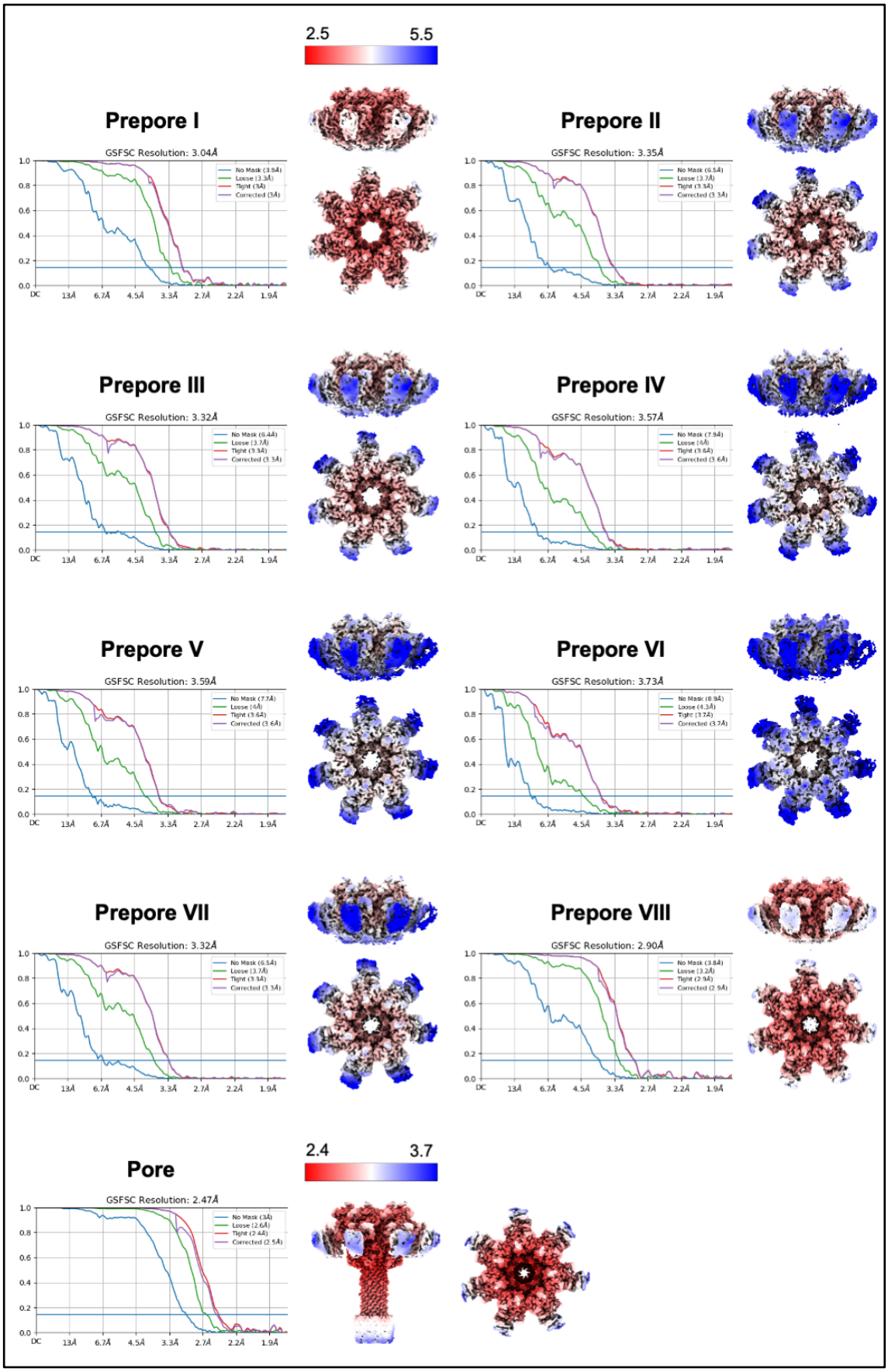
2.5
5.5
Prepore I
GSFSC Resolution: 3.04Å
Prepore II
GSFSC Resolution: 3.35Å
Prepore III
GSFSC Resolution: 3.32Å
Prepore IV
GSFSC Resolution: 3.57Å
Prepore V
GSFSC Resolution: 3.59Å
Prepore VI
GSFSC Resolution: 3.73Å
Prepore VII
GSFSC Resolution: 3.32Å
Prepore VIII
GSFSC Resolution: 2.90Å
Pore
GSFSC Resolution: 2.47Å
2.4
3.7

629

Extended Data Figure 3 | Global and local resolution

The global resolution was calculated using the gold-standard FSC threshold of 0.143. The local resolution was estimated with the RELION Local Resolution job using the final half-maps that are calculated using CryoSPARC. For Ib-prepore, the maps are coloured by the same resolution range (2.5 Å to 5.5 Å), while an independent resolution range coloured Ib-pore due to its outstanding resolution.

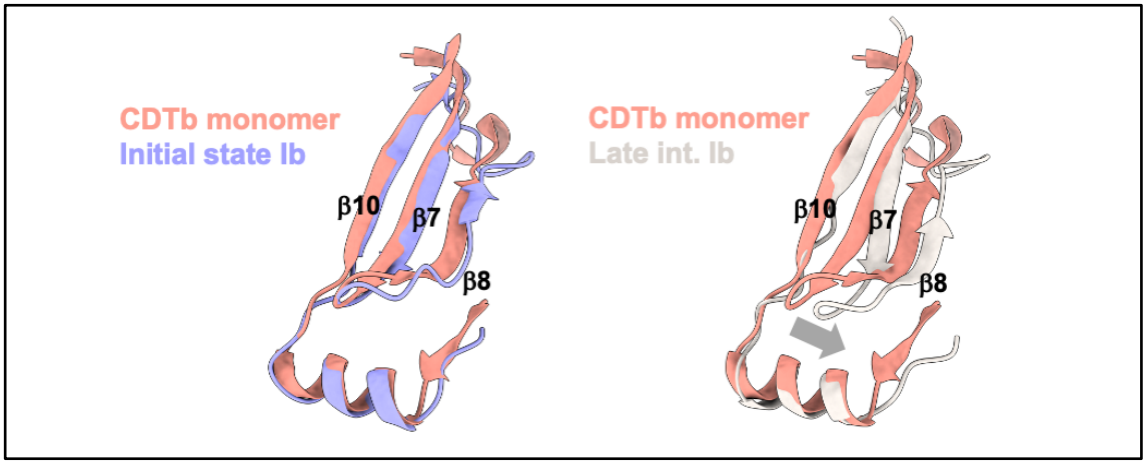

Extended Data Figure 4 | Structural comparison between Ib and CDTb monomer

The monomeric CDTb structure (PDBID: 8DCM) was aligned to the Ib Initial state from Prepore I and the Early int. from Prepore VII.

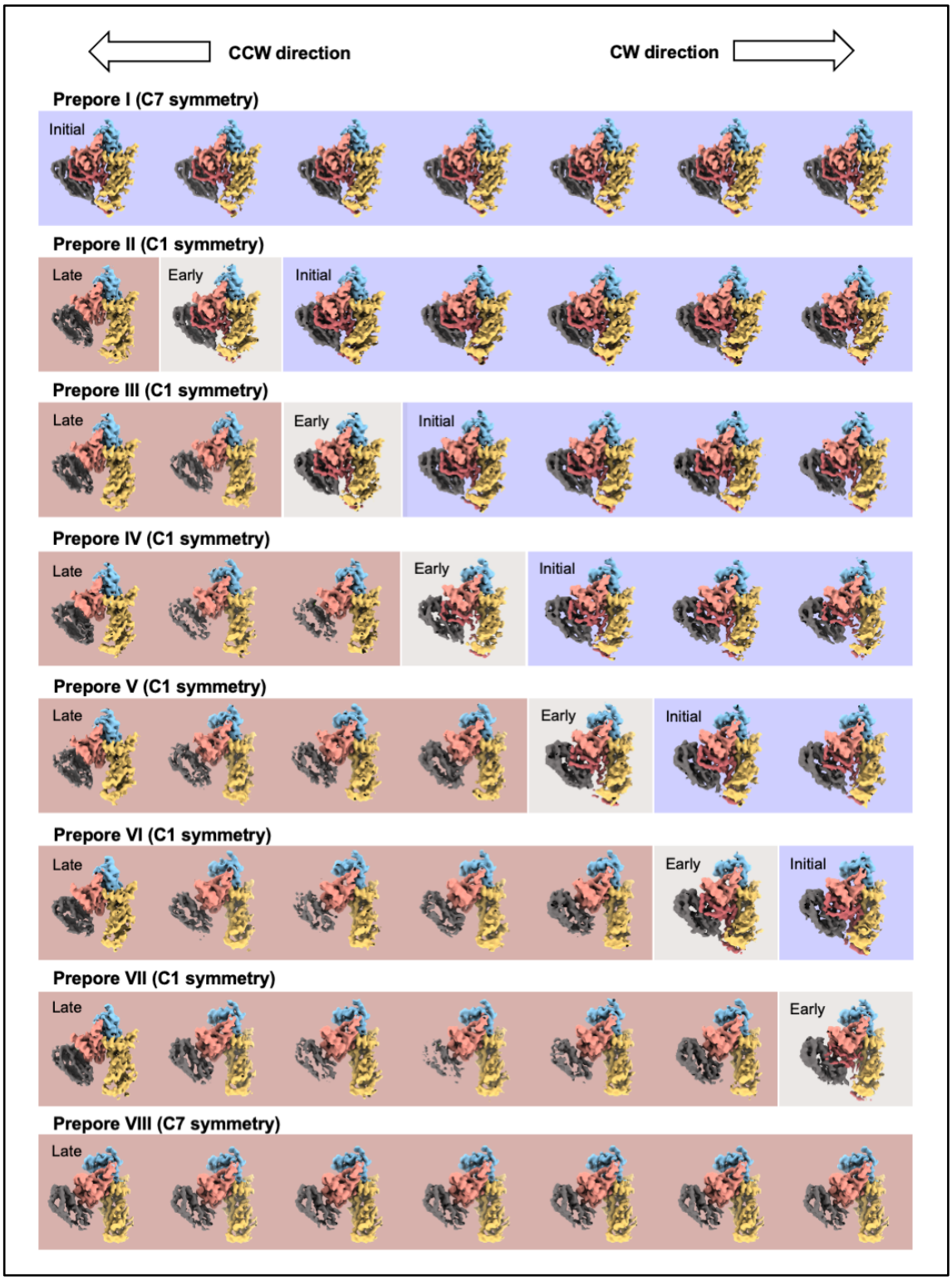

Extended Data Figure 5 | Protomers profile contained in oligomers

Density maps of the protomers were trimmed from their respective prepores, along with their atomic models. Owing to the symmetry for averaging, applied during the single particle analysis, all protomer maps from Prepore I and Prepore VIII are same. The CW and CCW

directions were defined relative to the top of the Ib oligomer where the Ia docking region was located.

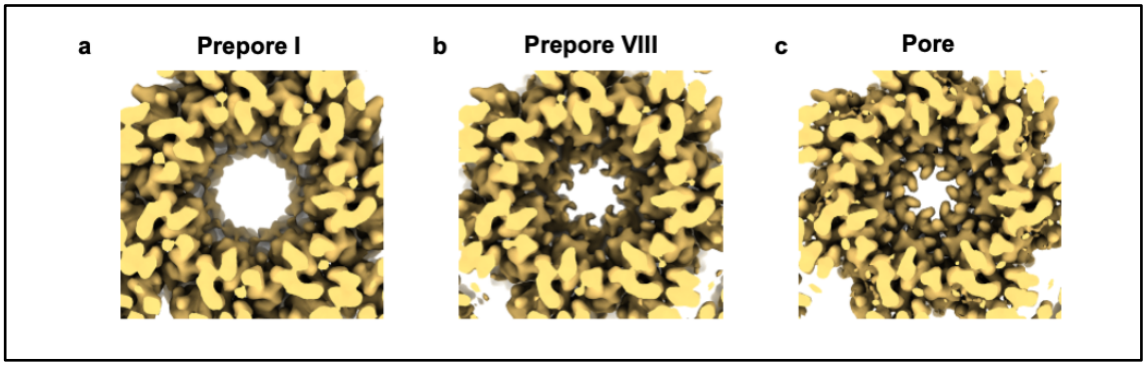

Extended Data Figure 6 | Comparison of the constriction-site top view

A close-up view of the central constriction site. Each map was calculated using C7 symmetry.

EMDB ID	Pore EMD-61772	Prepore I EMD-61771	Prepore II EMD-61774	Prepore III EMD-61773	Prepore IV EMD-61775	Prepore V EMD-61776	Prepore VI EMD-61777	Prepore VII EMD-61778	Prepore VIII EMD-61779
Magnification	81,000								
Voltage (kV)	300								
Electron Exposure ($e^-/Å^2$)	50								
Defocus Range (μm)	-0.6–1.6								
Pixel Size (Å)	0.88								
Symmetry Imposed	C7	C7	C1	C1	C1	C1	C1	C1	C7
Initial Particle Images (No.)	6,223,563								
Final Particle Images (No.)	161,249	10,511	15,199	22,352	8,878	11,285	7,676	23,305	17,097
Map Resolution (Å)	2.47	3.04	3.35	3.32	3.57	3.59	3.73	3.32	2.90
FSC Threshold	0.143								

Table1 1 | Cryo-EM data collection statistics

PDB ID	Pore 9JSG	Prepore I 9JSF	Prepore II 9JSI	Prepore III 9JSH	Prepore IV 9JSK	Prepore V 9JSL	Prepore VI 9JSM	Prepore VII 9JSN	Prepore VIII 9JSO
Refinement									
Model Resolution (Å)	2.6	3.2	3.6	3.6	3.6	3.7	4.1	3.6	3.2
FSC Threshold	0.5								
Model Composition									
Non-hydrogen Atoms	28,539	27,426	26,589	26,191	25,806	25,489	25,502	24,827	24,612
Protein Residues	3,710	3,563	3,453	3,397	3,343	3,299	3,256	3,207	3,171
Ligands	21	21	21	21	21	21	21	21	21
***B* factor**									
Protein ($Å^2$)	57.22	72.41	16.28	10.83	29.92	31.31	22.04	24.75	70.82
Ligand ($Å^2$)	60.40	60.85	10.12	6.43	24.55	24.25	61.32	19.90	52.98
R.M.S.Deviations									
Bond Lengths	0.008	0.005	0.003	0.005	0.003	0.004	0.005	0.004	0.003
Bond Angles	1.096	0.988	0.512	0.654	0.524	0.950	0.973	0.939	0.921
Validation									
MolProbity Score	1.36	1.62	1.65	1.81	1.69	1.56	1.75	1.48	1.54
Clash Score	3.69	5.33	6.76	8.58	7.19	4.54	9.49	4.06	5.84
Poor Rotamers (%)	0.80	0.22	0.00	0.03	0.03	0.10	0.07	0.04	0.25
Ramachandran Plot									
Favored (%)	96.73	95.23	95.94	94.98	95.75	95.26	96.30	95.83	96.63
Allowed (%)	3.27	4.77	4.06	5.02	4.25	4.71	3.70	4.14	3.37
Disallowed (%)	0.00	0.00	0.00	0.00	0.00	0.03	0.00	0.03	0.00

Table 2 | Refinement and validation statistics

666 **Reference**

667 1. Bischofberger, M., Iacovache, I. & van der Goot, F. G. Pathogenic pore-
668 forming proteins: function and host response. *Cell Host Microbe* **12**, 266–275 (2012).
669 2. Li, Y. *et al.* Structural Basis of the Pore-Forming Toxin/Membrane Interaction.
670 *Toxins* **13**, 128 (2021).
671 3. Simpson, L. L., Stiles, B. G., Zepeda, H. H. & Wilkins, T. D. Molecular basis
672 for the pathological actions of Clostridium perfringens iota toxin. *Infect. Immun.* **55**,
673 118–122 (1987).
674 4. Perelle, S., Gibert, M., Bourlioux, P., Corthier, G. & Popoff, M. R. Production
675 of a complete binary toxin (actin-specific ADP-ribosyltransferase) by Clostridium
676 difficile CD196. *Infect. Immun.* **65**, 1402–1407 (1997).
677 5. Popoff, M. R. & Boquet, P. Clostridium spiroforme toxin is a binary toxin
678 which ADP-ribosylates cellular actin. *Biochem. Biophys. Res. Commun.* **152**, 1361–
679 1368 (1988).
680 6. Aktories, K. *et al.* Botulinum C2 toxin ADP-ribosylates actin. *Nature* **322**,
681 390–392 (1986).
682 7. Liu, W. & Nestorovich, E. M. Anthrax toxin channel: What we know based on
683 over 30 years of research. *Biochim. Biophys. Acta BBA - Biomembr.* **1863**, 183715
684 (2021).
685 8. Knapp, O., Benz, R. & Popoff, M. R. Pore-forming activity of clostridial
686 binary toxins. *Biochim. Biophys. Acta BBA - Biomembr.* **1858**, 512–525 (2016).
687 9. Nagahama, M. *et al.* Clostridium perfringens Iota-Toxin b Induces Rapid Cell
688 Necrosis ▿ . *Infect. Immun.* **79**, 4353–4360 (2011).
689 10. Sakurai, J. & Kobayashi, K. Lethal and dermonecrotic activities of Clostridium
690 perfringens lota toxin: biological activities induced by cooperation of two nonlinked
691 components. *Microbiol. Immunol.* **39**, 249–253 (1995).
692 11. Stiles, B. G. & Wilkins, T. D. Purification and characterization of Clostridium
693 perfringens iota toxin: dependence on two nonlinked proteins for biological activity.
694 *Infect. Immun.* **54**, 683–688 (1986).
695 12. Gordon, V. M., Leppla, S. H. & Hewlett, E. L. Inhibitors of receptor-mediated
696 endocytosis block the entry of Bacillus anthracis adenylate cyclase toxin but not that of
697 Bordetella pertussis adenylate cyclase toxin. *Infect. Immun.* **56**, 1066–1069 (1988).
698 13. Barth, H. *et al.* Cellular uptake of Clostridium botulinum C2 toxin requires
699 oligomerization and acidification. *J. Biol. Chem.* **275**, 18704–18711 (2000).

14. Schering, B., Bärmann, M., Chhatwal, G. S., Geipel, U. & Aktories, K. ADP-ribosylation of skeletal muscle and non-muscle actin by Clostridium perfringens iota toxin. *Eur. J. Biochem.* **171**, 225–229 (1988).
15. Reuner, K. H., Presek, P., Boschek, C. B. & Aktories, K. Botulinum C2 toxin ADP-ribosylates actin and disorganizes the microfilament network in intact cells. *Eur. J. Cell Biol.* **43**, 134–140 (1987).
16. Duesbery, N. S. *et al.* Proteolytic Inactivation of MAP-Kinase-Kinase by Anthrax Lethal Factor. *Science* **280**, 734–737 (1998).
17. Leppla, S. H. Anthrax toxin edema factor: a bacterial adenylate cyclase that increases cyclic AMP concentrations of eukaryotic cells. *Proc. Natl. Acad. Sci.* **79**, 3162–3166 (1982).
18. Krantz, B. A. *et al.* A phenylalanine clamp catalyzes protein translocation through the anthrax toxin pore. *Science* **309**, 777–781 (2005).
19. Jiang, J., Pentelute, B. L., Collier, R. J. & Zhou, Z. H. Atomic structure of anthrax protective antigen pore elucidates toxin translocation. *Nature* **521**, 545–549 (2015).
20. Yamada, T. *et al.* Cryo-EM structures reveal translocational unfolding in the clostridial binary iota toxin complex. *Nat. Struct. Mol. Biol.* **27**, 288–296 (2020).
21. Kawamoto, A. *et al.* Cryo-EM structures of the translocational binary toxin complex CDTa-bound CDTb-pore from Clostridioides difficile. *Nat. Commun.* **13**, 6119 (2022).
22. Hardenbrook, N. J. *et al.* Atomic structures of anthrax toxin protective antigen channels bound to partially unfolded lethal and edema factors. *Nat. Commun.* **11**, 840 (2020).
23. Melnyk, R. A. & Collier, R. J. A loop network within the anthrax toxin pore positions the phenylalanine clamp in an active conformation. *Proc. Natl. Acad. Sci. U. S. A.* **103**, 9802–9807 (2006).
24. Sun, J., Lang, A. E., Aktories, K. & Collier, R. J. Phenylalanine-427 of anthrax protective antigen functions in both pore formation and protein translocation. *Proc. Natl. Acad. Sci.* **105**, 4346–4351 (2008).
25. Sellman, B. R., Nassi, S. & Collier, R. J. Point Mutations in Anthrax Protective Antigen That Block Translocation *. *J. Biol. Chem.* **276**, 8371–8376 (2001).
26. Scott, H. *et al.* Structure of the Anthrax Protective Antigen D425A Dominant Negative Mutant Reveals a Stalled Intermediate State of Pore Maturation. *J. Mol. Biol.* **434**, 167548 (2022).

735 27. Punjani, A., Rubinstein, J. L., Fleet, D. J. & Brubaker, M. A. cryoSPARC:
736 algorithms for rapid unsupervised cryo-EM structure determination. *Nat. Methods* **14**,
737 290–296 (2017).
738 28. Goldsmith, J. A., Dewar, V., Hermand, P., Blais, N. & McLellan, J. S.
739 Structural Basis for Binding of Neutralizing Antibodies to Clostridioides difficile
740 Binary Toxin. *J. Bacteriol.* **205**, e00456-22 (2023).
741 29. Petosa, C., Collier, R. J., Klimpel, K. R., Leppla, S. H. & Liddington, R. C.
742 Crystal structure of the anthrax toxin protective antigen. *Nature* **385**, 833–838 (1997).
743 30. Naik, S. *et al.* Monitoring the Kinetics of the pH-Driven Transition of the
744 Anthrax Toxin Prepore to the Pore by Biolayer Interferometry and Surface Plasmon
745 Resonance. *Biochemistry* **52**, 6335–6347 (2013).
746 31. Laver, W. G. & Valentine, R. C. Morphology of the isolated hemagglutinin and
747 neuraminidase subunits of influenza virus. *Virology* **38**, 105–119 (1969).
748 32. Gallagher, J. R. *et al.* Characterization of Hemagglutinin Antigens on Influenza
749 Virus and within Vaccines Using Electron Microscopy. *Vaccines* **6**, 31 (2018).
750 33. Xu, X. *et al.* Structure of the cell-binding component of the Clostridium
751 difficile binary toxin reveals a di-heptamer macromolecular assembly. *Proc. Natl. Acad.*
752 *Sci. U. S. A.* **117**, 1049–1058 (2020).
753 34. Anderson, D. M., Sheedlo, M. J., Jensen, J. L. & Lacy, D. B. Structural
754 Insights into the Transition of Clostridioides difficile Binary Toxin from Prepore to
755 Pore. *Nat. Microbiol.* **5**, 102–107 (2020).
756 35. Feld, G. K. *et al.* Structural basis for the unfolding of anthrax lethal factor by
757 protective antigen oligomers. *Nat. Struct. Mol. Biol.* **17**, 1383–1390 (2010).
758 36. Antoni, C. *et al.* Cryo-EM structure of the fully-loaded asymmetric anthrax
759 lethal toxin in its heptameric pre-pore state. *PLOS Pathog.* **16**, e1008530 (2020).
760 37. Zhou, K. *et al.* Atomic structures of anthrax prechannel bound with full-length
761 lethal and edema factors. *Struct. Lond. Engl. 1993* **28**, 879-887.e3 (2020).
762 38. Jiao, F. *et al.* Perforin-2 clockwise hand-over-hand pre-pore to pore transition
763 mechanism. *Nat. Commun.* **13**, 5039 (2022).
764 39. Rabideau, A. E., Liao, X., Akçay, G. & Pentelute, B. L. Translocation of Non-
765 Canonical Polypeptides into Cells Using Protective Antigen. *Sci. Rep.* **5**, 11944 (2015).
766 40. Punjani, A. & Fleet, D. J. 3D variability analysis: Resolving continuous
767 flexibility and discrete heterogeneity from single particle cryo-EM. *J. Struct. Biol.* **213**,
768 107702 (2021).

41. Rubinstein, J. L. & Brubaker, M. A. Alignment of cryo-EM movies of individual particles by optimization of image translations. *J. Struct. Biol.* **192**, 188–195 (2015).
42. Estimation of high-order aberrations and anisotropic magnification from cryo-EM data sets in RELION-3.1 - PubMed. https://pubmed.ncbi.nlm.nih.gov/32148853/.
43. Scheres, S. H. W. RELION: Implementation of a Bayesian approach to cryo-EM structure determination. *J. Struct. Biol.* **180**, 519–530 (2012).
44. Punjani, A., Zhang, H. & Fleet, D. J. Non-uniform refinement: adaptive regularization improves single-particle cryo-EM reconstruction. *Nat. Methods* **17**, 1214–1221 (2020).
45. Goddard, T. D. *et al.* UCSF ChimeraX: Meeting modern challenges in visualization and analysis. *Protein Sci. Publ. Protein Soc.* **27**, 14–25 (2018).
46. Emsley, P. & Cowtan, K. Coot: model-building tools for molecular graphics. *Acta Crystallogr. D Biol. Crystallogr.* **60**, 2126–2132 (2004).
47. Afonine, P. V. *et al.* Real-space refinement in PHENIX for cryo-EM and crystallography. *Acta Crystallogr. Sect. Struct. Biol.* **74**, 531–544 (2018).
48. Chen, V. B. *et al.* MolProbity: all-atom structure validation for macromolecular crystallography. *Acta Crystallogr. D Biol. Crystallogr.* **66**, 12–21 (2010).
49. Smart, O. S., Neduvelil, J. G., Wang, X., Wallace, B. A. & Sansom, M. S. P. HOLE: A program for the analysis of the pore dimensions of ion channel structural models. *J. Mol. Graph.* **14**, 354–360 (1996).